https://doi.org/10.2352/ISSN.2470-1173.2021.15.COIMG-291

Testing the Goodness of Model Fit in Tunable Diode Laser Absorption Tomography

Zeeshan Nadir1, Kristin M. Rice2, Michael S. Brown3, Charles A. Bouman1 1School of Electrical and Computer Engineering, Purdue University, West Lafayette, IN, 47907, USA 2 AFRL/RQHF, High Speed Systems Division, 676 Second Street, Arnold AFB, TN, 37389-4000 3 AFRL/RQHF, High Speed Systems Division, 2130 Eighth Street, Wright-Patterson AFB, OH, 45433-7542

Abstract

Tunable diode laser absorption tomography (TDLAT) has emerged as a popular nonintrusive technique for simultaneous sensing of gas concentration and temperature by making light absorbance measurements. Major challenge of TDLAT imaging is that the measurement data is very sparse. Therefore, precise models are required to describe the measurement process (forward model) and the behavior of the gas flow properites (prior model) to get accurate reconstructions.

The sparsity of the measurement data makes TDLAT very sensitive to the accuracy of the models and makes it prone to overfitting. Both the forward and prior models can have systematic errors due to several reasons. So far, substantial amount of work has been done by researchers on developing reconstruction methods and formulating models, forward and prior. Yet, there has not been significant research work done on constructing a metric for goodness of the model fit that can indicate when there is an inaccuracy in the forward or the prior model. In this paper, we present a metric for goodness of model fit that can be used to indicate if the models used in the reconstruction are inaccurate. Results show that our metric can reliably quantify the goodness of model fit for sparese data reconstruction problems such as TDLAT.

Introduction

Tunable diode laser absorption tomography (TDLAT) is a popular non-intrusive method to determine different properties of gaseous media in situ. [1–3]. In TDLAT imaging of gaseous flow, precisely tuned laser light is used to measure light absorption spectrum which is reconstructed to determine different properties simultaneously such as concentration and the temperature of the gas flow [4–6]. TDLAT has several advantages over conventional gas flow imaging techniques that include high signal to noise ratio, relative simplicity of the equipment [6–8] and specie-specific signals [9].

Unlike conventional image reconstruction problems such as X-Ray computed tomography (X-Ray CT), TDLAT poses many challenges including non-linearities and availability of a very small number of projection measurements [4]. In TDLAT imaging systems, typically there may be only 10-100 measurements available to estimate 1,000 to 10,000 unknown variables. Therefore, closed form solutions based on filtered back projection algorithm can not be used [10, 11]. A typical approach to TDLAT works by making use of simplifying assumptions to help constrain the solution such as assuming the availability of a large number of projection measurements [12, 13], assuming axisymmetric gas flow [14, 15] and assuming simple flow profiles [16]. These assumptions restrict the application of the typical approaches to a sparse reconstruction problem such as TDLAT.

Alternatively, reconstruction accuracy can be increased by model-based iterative reconstruction (MBIR) framework [7, 17]. In MBIR, a model is specified for both the measurement process (forward model) and for the unknown image to be reconstructed (prior model). While using model based methods in TDLAT gives a huge advantage in terms of reconstruction accuracy, it also makes them prone to producing inaccurate or biased reconstruction results if there are systematic errors in the models used for reconstruction. There are many sources of mismatches in the modeling process involved in TDLAT. For example, there can be error in the spectroscopic parameters used [18] which are continually updated. Additionally, the TDLAT measurement process may be subject to harsh environments in which physical vibrations may alter laser beam paths over time [19].

Since TDLAT reconstruction requires the inversion of very sparse amounts of data, it is very susceptible to errors resulting from forward modeling mismatch and data over fitting. Perhaps the closest work to the work presented in this paper is the work done by Mustafa et. al. on model validation in positron emission tomography (PET) [20]. However, they use a dense set of projection measurements and reconstruct the error sinograms using filtered back projection which is not applicable in this work.

In this paper, we present a systematic method of model validation in sparse data reconstruction problems while specifically using TDLAT as an application for experiments. Finding model mismatch is extremely crucial in applications which have limited measurement data and are highly prone to over-fitting and modeling errors. Because of sparsity of measurements, it is difficult to validate modeling errors by visualizing the error between measurements and forward projections. We propose to use a method based on the theory of statistical hypothesis testing by constructing a continuously varying metric that can be used to validate the reconstruction models; both forward and the prior. We analyze several aspects of the residual error and combine several hypothesis tests to increase the likelihood of detecting modeling errors. We perform several experiments using both correct and incorrect models to show the utility of our method. Experimental results show that our metric can reliably detect modeling errors in sparse data applications such as TDLAT.

Construction of Posterior Distribution

A classic approach to model based image reconstruction (MBIR) techniques is the computation of the maximum a posteriori (MAP) estimate which is obtained by maximizing the posterior distribution of the unknown signal given the measured data [21]. The MAP estimate is then given as follows

$$\hat{x} = \arg\max_{x} \left\{ \log p\left(Y|x\right) + \log p\left(x\right) \right\}, \tag{1}$$

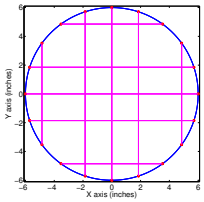

Figure 1. *Schematic of the region of interest and projection measurement paths. The magenta lines show the laser beam paths of projection measurements. Blue circle represents the boundary of the flowing medium. The red asterisks are source detector pairs. The region of interest is inside the blue circle.*

where $p(Y|x)$ is the forward model giving the probability of observing the measurement matrix Y given the unknown signal x, and $p(x)$ is the prior model giving the prior probability of observing x.

Forward Model

In TDLAT imaging [22, 23], projection measurements corresponding to a particular target molecule, in our case water, are made along a few projection paths and at a few discrete frequencies [7, 24]. Fig. 1 shows one such schematic of the projection paths. Let J be the total projection paths, let K be the total number of observed absorption lines, let $Y \in \mathbb{R}^{J\times K}$ be the light absorbance measurement matrix. Let $x = [N,\ T] \in \mathbb{R}^p$ be the vector of unknown molecular density, $N \in \mathbb{R}^{p/2}$, and temperature, $T \in \mathbb{R}^{p/2}$. The light absorbance projection measurements are typically corrupted by a variety of noise sources that include electronic noise, shot noise, digitization noise, beam steering, light scattering by particles and uncertainty in the spectroscopic database [18] all of which are modeled together as additive white Gaussian noise with mean 0 and variance σ^2. As a result, the relation between the measurements Y and unknown x is given by:

$$Y = H[F(x)] + W\ , \tag{2}$$

where $H \in \mathbb{R}^{J\times\frac{p}{2}}$ is the forward projection matrix, $F(x) = \left[f_1(x)\ f_2(x)\ \ldots\ f_K(x)\right] \in \mathbb{R}^{\frac{p}{2}\times K}$, where $f_k(x) = f_k(N,T) \in \mathbb{R}^{\frac{p}{2}}$ models the non-linear dependence of light absorption for a particular absorption line and $W \in \mathbb{R}^{J\times K}$ is the white noise matrix, $[W]_{j,k} \sim \mathcal{N}(0,\sigma^2)$. Combining this together, the log likelihood of the measurements Y given the unknown x is given by

$$\log p\left(Y|x\right) = -\frac{1}{2\sigma^2}\left\|Y - H\left[F(x)\right]\right\|_2^2 + \eta\ , \tag{3}$$

where the norm in equation (3) is Frobenius norm and η is a constant that does not depend on x.

Prior Model

We model the joint distribution of the molecular density N and the temperature T using a Gaussian mixture model (GMM) with M mixture components. GMM distribution allows for modeling both the long range correlations between the pixels of N and T and the non-homogeneous, non-Gaussian behaviors. The likelihood function of x is therefore given as follows:

$$p(x) = \sum_{m=1}^{M} \frac{\pi_m |B_m|^{\frac{1}{2}}}{\left(2\pi\right)^{\frac{p}{2}}} \exp\left\{-\frac{1}{2}\left\|x-\mu_m\right\|_{B_m}^2\right\}, \tag{4}$$

where π_m, μ_m represent the prior probability and mean of the class m and B_m represents the precision matrix of class m, equivalently the inverse of class covariance matrix R_m.

Typically, the dimension p of the unknown x can be several thousand. However, in the majority of cases, the unknown images reside on a very thin manifold in a higher dimensional space. Therefore we express x using an eigenimage basis set $E \in \mathbb{R}^{p\times\widetilde{p}}$ [25]

$$x = Ez\ , \tag{5}$$

where z is the equivalent representation of the unknown x in eigenimage basis set. In a typical scenario, the dimension $\widetilde{p}$ of the vector z is much smaller than the dimension p of the vector x. The vector z also has a Gaussian mixture distribution and its parameters are related to the parameters of x by the following equations,

$$\widetilde{\pi}_m = \pi_m, \tag{6}$$
$$\widetilde{\mu}_m = E^t\mu_m, \tag{7}$$
$$\widetilde{R}_m = E^t R_m E, \tag{8}$$

where $\widetilde{\pi}_m, \widetilde{\mu}_m, \widetilde{R}_m$ are the prior class probability, class mean and class covariance of the random vector z, and the class precision matrix of z is denoted by $\widetilde{B}_m$.

Posterior Distribution

The log posterior distribution of the vector z given the measurement data Y is constructed by combining the forward and the prior distributions as follows:

$$\log p(z|Y) = -\frac{1}{2\sigma^2}\left\|Y - Hf(Ez)\right\|_2^2 + \log\left(\sum_{m=1}^{M}\frac{\widetilde{\pi}_m|\widetilde{B}_m|^{\frac{1}{2}}}{\left(2\pi\right)^{\frac{\widetilde{p}}{2}}}\exp\left\{-\frac{1}{2}\left\|z-\widetilde{\mu}_m\right\|_{\widetilde{B}_m}^2\right\}\right) + \varepsilon, \tag{9}$$

where all the terms not dependent on z are merged in ε.

Methods

Using the posterior distribution of eq. 9, we compute the MAP estimate of the unknown molecular density and temperature and use them to compute the residual error between predicted and measured values of the absorbance spectrum. We hypothesize that if the reconstruction is accurate then the residual error should appear to be a sample of white Gaussian noise. If the residual error seems unlikely to be a sample of white Gaussian noise then we conclude that our reconstruction is incorrect likely because of an inaccurate posterior distribution.

To this end, we use four different hypothesis tests; Wald Wolfwitz (WW) runs test [26], up and down (UD) runs test [27], Kolmogorov Smirnov test [28] and Binomial test [29]. For each hypothesis test, we compute the so called p-value [30] that gives the probability of observing the data given that the null hypothesis is true. We combine the hypotheses using Fisher's method [31] and construct our final p-value metric, p_f. To reject the null hypothesis, we require p_f be smaller than the threshold value of 0.1 (significance level) [32].

Runs Test

We use two different types of runs test to determine if the samples of the residual error appear to be independent and identically distributed or not. Both these tests compute the so called

"number of runs" which are normally distributed under the null hypothesis with means and variances computed from the given data.

Typically, Wald-Wolfwitz (WW) runs test is performed on a given 1-D binary sequence [1]. Since our residual error is continuously distributed, we convert it in to a binary sequence by comparing each residual error with the presumed mean value of zero. For WW runs test, a run is defined as a contiguous sub-sequence of the binary numbers all having the same sign.

The up and down (UD) runs tests is generally more effective in testing for serial correlations in the data. For a given numeric sequence, an up and down run is defined as a subsequence of increasing or decreasing numbers. If the dataset consists of independent samples of a distribution, then we neither expect to see any increasing or decreasing trends in the sample, nor do we expect to see a periodic trends in the data.

We compute the p-values for these two tests from the number of runs as given in the following equation:

$$p_k = P\left(|z| > \frac{|R_k - \mu_k|}{\sigma_k}\right) , \tag{10}$$

where $k \in \{1,2\}$, p_1 and p_2 are the associated p-values of WW runs test and UD runs test respectively, R_1, R_2 are the observed number of runs for the two tests, and μ_1, μ_2 and σ_1, σ_2 are the associated means and standard deviations of WW runs test and UD runs test respectively computed under the assumption of null hypotheses of these two tests [26, 27].

Kolmogorov Smirnov Test

We model the noise in our TDLAT measurements as white Gaussian noise with mean 0 and variance σ^2. If the reconstruction is accurate, then the empirical distribution of the residual error is expected to be similar to $\mathcal{N}\left(0, \sigma^2\right)$. To validate the distribution of the residual error we use Kolmogorov Smirnov (KS) test [28, 33, 34]. KS test works computing the empirical cumulative distribution function (CDF), $F_n(\tau)$ of the normalized residual error and comparing it with the presumed CDF, $F(\tau)$ i.e., CDF of $\mathcal{N}(0,1)$. A distance metric, D_n, given by the maximum absolute difference between $F_n(x)$ and $F(x)$ is then computed as given below:

$$D_n = \max_x |F_n(x) - F(x)| . \tag{11}$$

Under the null hypothesis that the normalized residual error is a sample drawn from $\mathcal{N}(0,1)$, the statistic $\sqrt{n}D_n$ follows Kolomogorov distribution [34]. The CDF of the Kolmogorov distribution is used to compute the p-value for this test as follows:

$$p_3 = 1 - K(\sqrt{n}\, D_n) , \tag{12}$$

where $K(\tau)$ is the Kolmogorov CDF.

Binomial Test

We test whether or not the residual error has roughly the same number of positive and negative errors in it. For this, we use Binomial test for the hypothesis that the residual error has a median value of zero [29, 35, 36]. For an unbiased residual error, we expect to see roughly an equal number of positive and negative errors.

To perform the binomial test, we compare each of the samples of the residual error from the assumed median value of zero. We call the number of observed positive errors B_p. If the true median value of the residual error is 0, then B_p shall have an asymptotic normal distribution. We compute the p-value for this test as follows:

$$p_4 = P\left(|z| > \frac{|B_p - \mu_B|}{\sigma_B}\right) , \tag{13}$$

where z is the standard normal random variable and μ_B and σ_B are computed from the residual error data under the assumption that the null hypothesis is true [37].

Combining all Hypotheses using Fisher's Method

In order to summarize the results from all the tests, we combine all the individual four tests using Fisher's method [31, 38]. The test statistic for Fisher's method is given by adding the negative log of the p-values:

$$W = \sum_{i=1}^{t} -2\log(p_i) , \tag{14}$$

where p_i is the p-value associated with the i^{th} test and t is the total number of tests (4 in our case).

It follows that under the null hypothesis that all t null hypothesis are true, W follows a chi-squared distribution with $2t$ degrees of freedom. We calculate the final p-value, p_f, by computing the following probability:

$$p_f = P\left(\chi_8^2 \geq W\right) , \tag{15}$$

where χ_8^2 is chi-squared random variable with 8 degrees of freedom and W is the statistic calculated using eq. 14. Having one or more of very small p-values, p_i, results in small value of the final p-value metric p_f leading to the rejection of our final null hypothesis.

Results

The posterior model is constructed from both the forward model and the prior model and an inaccuracy in either the forward model or the prior model can result in an inaccurate posterior model. We study these two problems (incorrect forward model and incorrect prior model) separately. In all the reconstruction experiments, we use iterative coordinate descent algorithm with eigen-images as the bases set [25]. Since the temperature and concentration have different units and dynamic ranges, we normalize their reconstruction errors with the dynamic range of the ground truth phantoms when presenting the results [25].

Identification of Inaccuracy in the Posterior Distribution due to Inaccurate Prior Model

In this experiment, we use the p-value metric p_f to identify the inaccuracy in the posterior distribution resulting from an inaccurate prior model. We construct an inadequate prior model by training a Gaussian mixture model (GMM) using an incomplete training dataset. We use eigen-images as our basis set for reconstruction (see eq. 9). The training data for the Gaussian mixture

[1] Both WW Runs test and UD runs test require a 1-D sequence. We convert the 2-D, $J \times K$ residual error matrix into two 1-D sequences by first reading all the columns contiguously and then reading all the rows contiguously. We compute the p-values for each of the two 1-D sequences separately and then take their geometric mean as our p-value for the test.

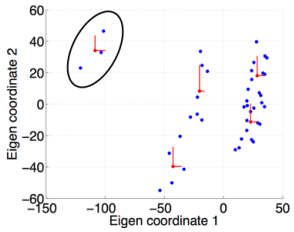

Figure 2. *Illustration of the scatter plot of the 42 CFD phantoms using the first two eigenimage basis vectors [25]. Blue dots represent the samples, red dots represent the mean of the cluster and the lengths of the red line segments are equal to the standard deviation of the samples in the respective cluster. The three phantoms inside the ellipse are part of the same cluster and are kept out of the training set.*

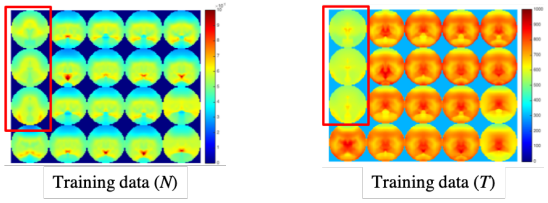

Figure 3. *Examples of CFD phantoms. The three phantoms in the red box represent the test cases, whereas, the remaining phantoms are a subset of the 39 phantoms that are used for training. There are no phantoms in the training set which are similar to the test phantoms. The scale of N is 0 to 10×10^{17} in units of molecules/cm^3, and the scale of temperature is 0 to 1000 in units of Kelvins.*

model comes from computational fluid dynamics (CFD) simulations.

We use a total of 42 CFD phantoms out of which, we use 3 as the test set as shown in fig. 2. As demonstrated in figure 3, the three phantoms that are kept outside of the training data have a distinctly different structure and dynamic range as compared to the rest of the phantoms that are used as training data and can not be modeled well by the remaining phantoms. We use these three phantoms as our test set. By training the mixture model on an incomplete training data, we construct an incorrect posterior distribution.

For one of the test case phantoms, we generate five sets of simulated absorbance measurement data by forward projecting the CFD phantom. For generating the forward projections, we use the layout of fig. 1 and four absorption features [25]. We simulate noise in the measurements as additive white Gaussian noise with standard deviation of the noise selected to yield an average signal to noise ratio of 30dB. We reconstruct all the five datasets and for each reconstruction, we vary the regularization level of the reconstruction by varying the influence of the prior model. For each regularization level, we compute an average of the metric p_f and the percent normalized root mean squared error (NRMSE) over the five measurement datasets. For comparison, we perform the same experiment using a Gaussian Markov random field distribution as the prior model [39] with 8 point neighborhood system.

Figure 4 shows the plot of the average p-value metric p_f and the average percent NRMSE for the two prior models. For the GMM prior, the values of p_f are extremely small, well below the threshold and the values of percent NRMSE are large. For

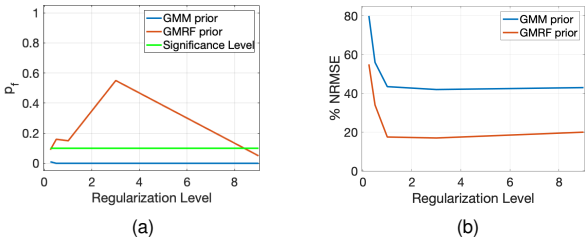

Figure 4. *Plots of p-value metric p_f and % NRMSE for GMM and GMRF prior models. The green curve shows the significance level for the rejection of null hypothesis which we choose as 0.1.*

the GMRF prior, the value of p_f are above the threshold and the percent NRMSE are much smaller when compared with GMM prior. For GMRF prior, the value of p_f above the threshold level indicates that our metric does not identify a possible inaccuracy in the posterior distribution. However, for the case of GMM prior, our metric identifies the inadequacy of the posterior distribution.

We also provide the reconstruction results for the two prior models in fig. 5 for one of the simulated datasets. It is clear from the figure that GMM prior overfits the insufficient training data leading to incorrect reconstruction result. The GMRF prior on the other hand does not produce artifacts. The p-value metric p_f for this GMM reconstruction is well below the threshold indicating an incorrect posterior distribution (resulting from a prior model which is over-fit to the training data).

Identification of Inaccuracy in the Posterior Distribution due to Inaccurate Forward Model

In this experiment, we use the p-value metric p_f to identify the inaccuracy in the posterior distribution resulting from an inaccurate forward model. We construct an incorrect forward model by changing the location of one of the projection paths by 2.13 inches to the right. This models a scenario where the projection paths drifted due to human error or vibrations in the system. The actual projection paths that are used to generate the projection measurements are given in figure 6(a) whereas the projection paths that are used to generate the reconstruction are given in figure 6(b). Notice that the first projection path has different location in the two figures.

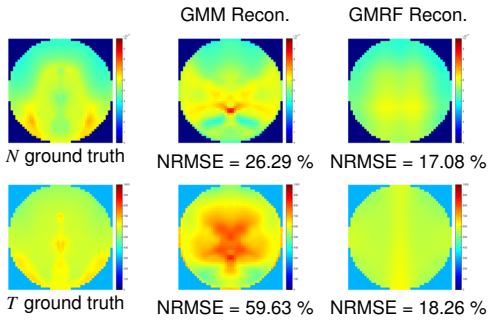

Figure 5. *Reconstruction results using two different prior distributions. GMM prior was constructed using non-representative training samples. For GMM prior, $p_f = 10^{-5}$ and for GMRF prior, $p_f = 0.55$. For each reconstruction, the regularization was tuned to maximize p_f.*

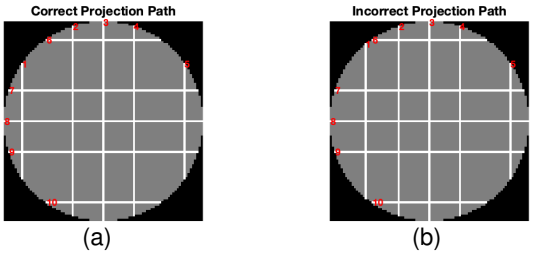

Figure 6. *The two projection paths are shown side by side. Grey color shows the pixels that are reconstructed whereas the white color shows the pixels through which a projection path passes. The 1st projection path in (b) is moved to the right by 2.13 inches.*

To perform the reconstruction experiment, we use a total of 114 CFD simulated phantoms. Out of these, one of the CFD phantoms is used as test set whereas the remaining are used as training data for the prior model. We train a Gaussian mixture distribution as the prior model and perform the reconstruction using eigen-image basis vectors. For the test case CFD phantom, given in figure, we generate the simulated projection measurements using the layout of figure 6(a) and four absorption features [25]. To simulate noise in the projection measurements, we add additive white Gaussian noise in the forward projections to yield an average SNR of 30dB. After the simulated projection measurements are generated, we use the layout of figure 6(b) in the reconstruction algorithm.

Figure 7 shows the ground truth CFD test phantom, the two reconstruction results using correct and incorrect measurement layout and the two forward projections using correct and incorrect layout. The reconstruction obtained with the incorrect layout (fig. 7 (f),(i)) shows artifacts, however, such artifacts can be difficult to identify in the absence of ground truth. We show the histogram of the noramlized residual error in fig. 8 for the two reconstructions along with the value of the metric p_f. The metric p_f takes a small value due to the unexpectedly large residual error in the first projection path which can also be seen visually in fig. 7(c) and fig. 8(b). Our p-value metric p_f accurately identifies the resulting incorrect posterior distribution due to incorrect forward model used.

Summary

In this paper, we proposed a scheme for finding deficiencies in the posterior distribution/model by developing a p-value metric p_f using the theory of statistical hypothesis testing. We used four different hypothesis tests increasing the power of our metric. We aggregated the results from the four tests to formulate the metric p_f. We showed that this metric p_f can be used to identify inaccuracies in the posterior model due to both incorrect forward or the incorrect prior models. Results in this paper demonstrate that the metric can be used as a reliable way to find cases where posterior distribution is incorrect.

Acknowledgment

The authors would like to thank Dr. Mark Hagenmaier of the Air Force Research Laboratory, Wright-Patterson AFB, OH for use of the CFD solutions. The authors would also like to thank the financial support provided by High Speed Systems Test program at AEDC (Ed Tucker Executing Agent) and the Air Force Office of Scientific Research.

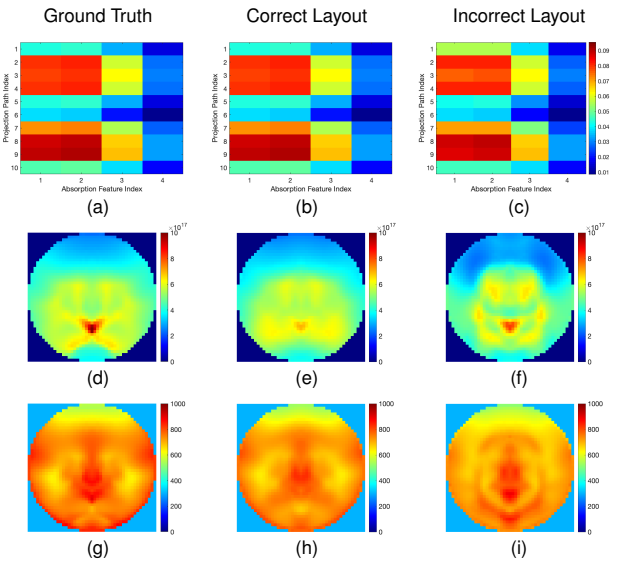

Figure 7. *(a) is the simulated measurement projeciton measurement dataset. (b) and (c) represent the forward projections using correct and incorrect layout respectively. (d), (e) and (f) show the ground truth concentration and the reconstructions of concentration using correct and incorrect layout respectively. (g), (h) and (i) show the ground truth temperature and the reconstructions of temperature using correct and incorrect layout respectively.*

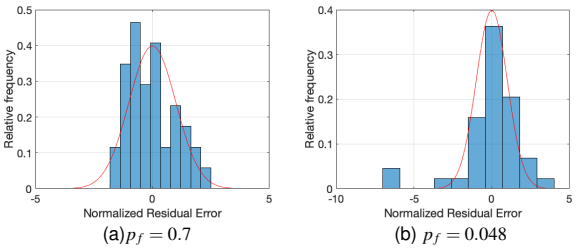

Figure 8. *(a) Histogram of normalized residual error with correct posterior distribution. (b) Histogram of normalized residual error with incorrect posterior distribution resulting from incorrect forward model. A standard normal PDF is overlaid on both the histograms in red color. Notice the large error values in (b) causing a small p-value.*

References

[1] C. Wang, "Laser applications to turbulent reactive flows; density measurement by resonance absorption and resonance scattering techniques," *Combustion Science and Technology*, vol. 13, no. 1-6, pp. 211–227, 1976.

[2] P. Emmerman, R. Goulard, R. Santoro, and H. Semerjian, "Multiangular absorption diagnostics of a turbulent argon-methane jet," *Journal of Energy*, vol. 4, no. 2, pp. 70–77, 1980.

[3] H. SEMERJIAN and S. RAY, "Laser tomography for simultaneous concentration and temperature measurement in reacting flows," in *AIAA 18th Thermophysics Conference, Montreal Canada*, 1983.

[4] M. S. Brown, G. C. Herring, K. Cabell, N. Hass, T. F. Barhorst, and M. Gruber, "Optical measurements at the combustor exit of the hifire 2 ground test engine," *AIAA Paper*, 2012.

[5] M. L. C. Z. Nadir, M. S. Brown and C. A. Bouman, "Gaussian mixture prior models for imaging of flow cross sections from sparse hyperspectral measurements," in *2015 IEEE Global Conference on Signal and Information Processing (GlobalSIP)*, Dec 2015, pp. 527–531.

[6] L. Ma and W. Cai, "Numerical investigation of hyperspectral tomography for simultaneous temperature and concentration imaging," *Applied optics*, vol. 47, no. 21, pp. 3751–3759, 2008.

[7] Z. Nadir, M. S. Brown, M. L. Comer, and C. A. Bouman, "Tomographic reconstruction of flowing gases using sparse training," in *2014 IEEE International Conference on Image Processing (ICIP)*, Oct 2014, pp. 1733–1737.

[8] M. G. Allen, "Diode laser absorption sensors for gas-dynamic and combustion flows," *Measurement Science and Technology*, vol. 9, no. 4, p. 545, 1998.

[9] M. Allen, E. Furlong, and R. Hanson, "Tunable diode laser sensing and combustion control," *Applied Combustion Diagnostics*, pp. 479–498, 2002.

[10] A. C. Kak and M. Slaney, *Principles of computerized tomographic imaging*. Siam, 1988, vol. 33.

[11] J. Hsieh, *Computed tomography: principles, design, artifacts, and recent advances*. SPIE press, 2009.

[12] M. Ravichandran and F. Gouldin, "Retrieval of asymmetric temperature and concentration profiles from a limited number of absorption measurements," *Combustion science and technology*, vol. 60, no. 1-3, pp. 231–248, 1988.

[13] B. Gillet, Y. Hardalupas, C. Kavounides, and A. Taylor, "Infrared absorption for measurement of hydrocarbon concentration in fuel/air mixtures (mast-b-liquid)," *Applied thermal engineering*, vol. 24, no. 11, pp. 1633–1653, 2004.

[14] C. Liu, L. Xu, and Z. Cao, "Measurement of axisymmetric temperature distributions using single view fan-beam tdlas tomography," in *Instrumentation and Measurement Technology Conference (I2MTC), 2013 IEEE International*, May 2013, pp. 876–879.

[15] F. Wang, K. Cen, N. Li, J. B. Jeffries, Q. Huang, J. Yan, and Y. Chi, "Two-dimensional tomography for gas concentration and temperature distributions based on tunable diode laser absorption spectroscopy," *Measurement Science and Technology*, vol. 21, no. 4, p. 045301, 2010.

[16] X. Liu, J. B. Jeffries, and R. K. Hanson, "Measurement of non-uniform temperature distributions using line-of-sight absorption spectroscopy," *AIAA journal*, vol. 45, no. 2, pp. 411–419, 2007.

[17] Z. Yu, J. Thibault, C. A. Bouman, K. D. Sauer, and J. Hsieh, "Fast model-based x-ray ct reconstruction using spatially nonhomogeneous icd optimization," *Image Processing, IEEE Trans. on*, vol. 20, no. 1, pp. 161–175, 2011.

[18] L. S. Rothman, D. Jacquemart, A. Barbe, D. Chris Benner, M. Birk, L. Brown, M. Carleer, C. Chackerian Jr, K. Chance, L. e. a. Coudert *et al.*, "The hitran 2004 molecular spectroscopic database," *Journal of Quantitative Spectroscopy and Radiative Transfer*, vol. 96, no. 2, pp. 139–204, 2005.

[19] C. D. Lindstrom, K. R. Jackson, S. Williams, R. Givens, W. F. Bailey, C.-J. Tam, and W. F. Terry, "Shock-train structure resolved with absorption spectroscopy part i: System design and validation," *AIAA Journal*, vol. 47, no. 10, pp. 2368–2378, 2009.

[20] M. E. Kamasak, B. T. Christian, C. A. Bouman, and E. D. Morris, "Quality and precision of parametric images created from pet sinogram data by direct reconstruction: proof of concept," *IEEE transactions on medical imaging*, vol. 33, no. 3, pp. 695–707, 2014.

[21] C. A. Bouman and K. Sauer, "A unified approach to statistical tomography using coordinate descent optimization," *Image Processing, IEEE Trans. on*, vol. 5, no. 3, pp. 480–492, 1996.

[22] V. Kasyutich and P. Martin, "Towards a two-dimensional concentration and temperature laser absorption tomography sensor system," *Applied Physics B*, vol. 102, no. 1, pp. 149–162, 2011.

[23] K. M. Busa, B. E. Rice, J. C. McDaniel, C. P. Goyne, R. D. Rockwell, J. A. Fulton, J. R. Edwards, and G. S. Diskin, "Direct measurement of combustion efficiency of a dual-mode scramjet via tdlat and spiv," in *53rd AIAA Aerospace Sciences Meeting*, Jan 2015.

[24] C. Lindstrom, C.-J. Tam, R. Givens, D. Davis, and S. Williams, "Diode laser absorption tomography using data compression techniques," in *Electronic Imaging 2008*. International Society for Optics and Photonics, 2008, pp. 68 140W–68 140W.

[25] Z. Nadir, M. S. Brown, M. L. Comer, and C. A. Bouman, "A model-based iterative reconstruction approach to tunable diode laser absorption tomography," *IEEE Transactions on Computational Imaging*, vol. 3, no. 4, pp. 876–890, Dec 2017.

[26] A. Wald and J. Wolfowitz, "On a test whether two samples are from the same population," *The Annals of Mathematical Statistics*, vol. 11, no. 2, pp. 147–162, 1940.

[27] R. Grafton, "Algorithm as 157: The runs-up and runs-down tests," *Journal of the Royal Statistical Society. Series C (Applied Statistics)*, vol. 30, no. 1, pp. 81–85, 1981.

[28] R. Wilcox, "Kolmogorov–smirnov test," *Encyclopedia of biostatistics*, 2005.

[29] H. Abdi, "Binomial distribution: binomial and sign tests," *Encyclopedia of measurement and statistics*, vol. 1, 2007.

[30] M. L. Tiku and A. D. Akkaya, *Robust estimation and hypothesis testing*. New Age International, 2004.

[31] R. A. Fisher, *Statistical methods for research workers*. Genesis Publishing Pvt Ltd, 1925.

[32] R. R. Wilcox, *Introduction to robust estimation and hypothesis testing*. Academic press, 2011.

[33] F. J. Massey Jr, "The kolmogorov-smirnov test for goodness of fit," *Journal of the American statistical Association*, vol. 46, no. 253, pp. 68–78, 1951.

[34] J. Wang, W. W. Tsang, and G. Marsaglia, "Evaluating kolmogorov's distribution," *Journal of Statistical Software*, vol. 8, no. 18, 2003.

[35] W. J. Dixon and A. M. Mood, "The statistical sign test," *Journal of the American Statistical Association*, vol. 41, no. 236, pp. 557–566, 1946.

[36] D. C. Howell, *Statistical methods for psychology*. Cengage Learning, 2012.

[37] A. Leon-Garcia, "Probability, statistics, and random processes for electrical engineering," 2017.

[38] R. Elston, "On fisher's method of combining p-values," *Biometrical journal*, vol. 33, no. 3, pp. 339–345, 1991.

[39] C. Bouman and K. Sauer, "A generalized gaussian image model for edge-preserving map estimation," *Image Processing, IEEE Trans. on*, vol. 2, no. 3, pp. 296–310, Jul 1993.

JOIN US AT THE NEXT EI!

IS&T International Symposium on

Electronic Imaging

SCIENCE AND TECHNOLOGY

Imaging across applications . . . Where industry and academia meet!

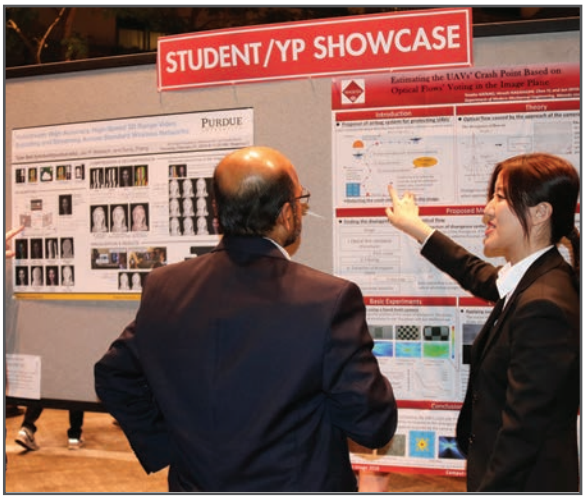

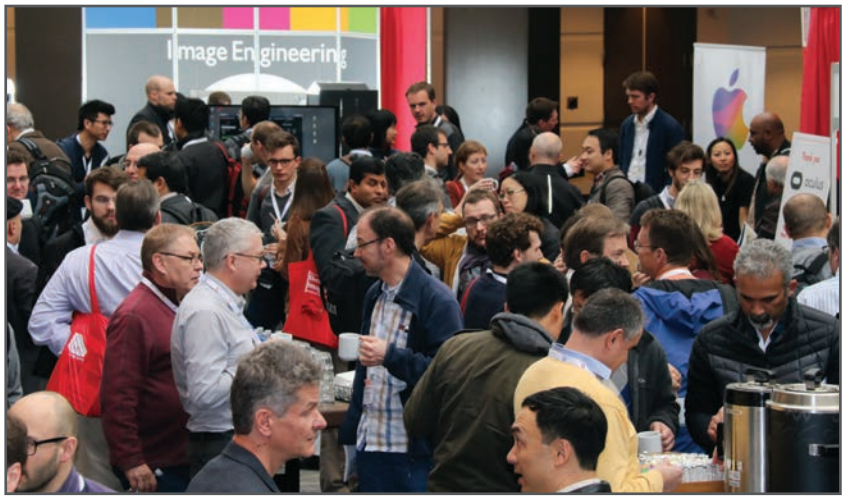

• SHORT COURSES • EXHIBITS • DEMONSTRATION SESSION • PLENARY TALKS •
• INTERACTIVE PAPER SESSION • SPECIAL EVENTS • TECHNICAL SESSIONS •

www.electronicimaging.org

IS&T
imaging.org